

PAPER



Cite this: *Phys. Chem. Chem. Phys.*,
2019, 21, 11385

Theoretical study of the $F(^2P) + NH_3 \rightarrow HF + NH_2$ reaction on an accurate potential energy surface: dynamics and kinetics†

Li Tian,^{ab} Yongfa Zhu,^{id ac} Hongwei Song^{id *a} and Minghui Yang^{id a}

The highly exothermic hydrogen abstraction reaction of the F atom with NH_3 is investigated using the quasi-classical trajectory method on a newly developed potential energy surface (PES) for the ground electronic state. The full-dimensional PES is constructed by fitting 41282 *ab initio* energy points at the level of UCCSD(T)-F12/aug-cc-pVTZ. The flexible fundamental invariant-neural network method is applied in the fitting, resulting in a total root mean square error of 0.13 kcal mol⁻¹. On one hand, the calculated differential cross sections agree reasonably well with the experimental results and indicate that the reaction is dominated by the direct abstraction and stripping mechanisms while a considerable amount of reaction takes place by the indirect “yo-yo” mechanism. The product energy partition also reproduces well the experimental result, which can be understood according to the geometry change along the minimum energy path. On the other hand, the obtained vibrational state distribution of the product HF follows $P_{\nu_{HF}=2} \approx P_{\nu_{HF}=1} > P_{\nu_{HF}=0} > P_{\nu_{HF}=3}$, less consistent with the scattered experimental results. In addition, the calculated thermal rate coefficients have practically no temperature dependence within the statistical errors.

Received 15th April 2019,
Accepted 13th May 2019

DOI: 10.1039/c9cp02113b

rsc.li/pccp

1. Introduction

The hydrogen abstraction reaction of fluorine atom with ammonia poses a big challenge to both experimental and theoretical studies. On one hand, the title reaction is very fast and accompanied by the secondary hydrogen abstraction reaction, $F + NH_2 \rightarrow HF + NH$ reaction, which proceeds even faster. Thus, traditional experimental techniques can't eliminate effects of the secondary reaction.^{1,2} On the other hand, the title reaction is highly exothermic, and presents a very low submerged barrier. An accurate description of the barrier requires high-level quantum chemistry calculations.^{3,4} It has been realized recently that this kind of barrier sometimes plays an important role in reaction dynamics.^{5–12}

Although much attention has been paid to investigate the dynamics and kinetics of the $F + NH_3 \rightarrow HF + NH_2$ reaction in the past several decades, controversies among different experiments, such as the vibrational distribution of the product HF

and the temperature dependence of rate coefficients, have not been settled.^{2,13–16} The vibrational distribution of HF has been determined using both low-pressure infrared chemiluminescence and flowing afterglow techniques. The results roughly fell into two categories: the first is a vibrationally cold distribution with $P(\nu_{HF} = 1) > P(\nu_{HF} = 2)$;^{2,14} the second is a vibrationally inverted distribution with $P(\nu_{HF} = 1) < P(\nu_{HF} = 2)$.¹³ The inverted distribution is always accompanied by excitations to $\nu_{HF} = 3$. The rate coefficients were reported by Walther and Wagner to show a positive temperature dependence at temperatures lower than 900 K and become almost temperature independent as the temperature further increases.¹⁵ In contrast, Persky obtained a negative temperature dependence from 276 K to 327 K in the experiment.¹⁶ Besides, Xiao *et al.* carried out crossed beams studies on the dynamics of the F-atom reaction with NH_3 and ND_3 . They found that the HF and DF products are mainly forward-scattered relative to the F-atom beam direction while the sideways- and backward-scattered products are nonnegligible.¹⁷

Theoretically, Espinosa-García and Corchado developed a full-dimensional analytical potential energy surface (PES) for the $F + NH_3 \rightarrow HF + NH_2$ reaction, namely PES-1997.¹⁸ The reactant and product properties from experiments and the calculated properties of a hydrogen-bonded complex linking $NH_2 \cdot HF$ were used to calibrate the PES. Then, quasi-classical trajectory (QCT) calculations based on the PES were performed

^a State Key Laboratory of Magnetic Resonance and Atomic and Molecular Physics, Wuhan Institute of Physics and Mathematics, Chinese Academy of Sciences, Wuhan 430071, China. E-mail: hwsong@wipm.ac.cn

^b College of Physical Science and Technology, Huazhong Normal University, Wuhan 430079, China

^c University of Chinese Academy of Sciences, Beijing 100049, China

† Electronic supplementary information (ESI) available. See DOI: 10.1039/c9cp02113b

to study the reaction mechanism of the $F + NH_3$ and $F + ND_3$ reactions.¹⁹ The calculated differential cross sections (DCSSs) reproduced reasonably well the experimental results. However, the agreement between theoretical and experimental product energy partitions was slightly poor, which was attributed to an excessively attractive character of the stretching terms in the analytical expression of the PES. In addition, thermal rate coefficients were calculated on the PES using both ring polymer molecular dynamics and QCT methods and exhibited practically no temperature dependence in the temperature range of 276–327 K.²⁰

In this work, we will develop a global, full-dimensional *ab initio* ground-state PES for the $F + NH_3 \rightarrow HF + NH_2$ reaction using the fundamental-invariant neural network (FI-NN) method. QCT calculations will then be performed on the PES to study the dynamics and kinetics of the reaction, aiming at unveiling the underlying reaction mechanism. The paper is organized as follows. Section II outlines the details of the *ab initio* calculations and PES fitting. The QCT and normal mode analysis (NMA) methods are given briefly in Section III, followed by the results and discussions in Section IV. Finally, the conclusions are supplied in Section V.

II. Potential energy surface

To develop an accurate full-dimensional PES for polyatomic systems with reasonable computational cost, much effort should be put to choose the *ab initio* method, the sampling scheme and the fitting tool. The *ab initio* method is determined as follows. The geometries and energies of the stationary points along the reaction path are calculated by different levels of *ab initio* method and basis sets, including UCCSD(T)/aug-cc-pVTZ, UCCSD(T)-F12/aug-cc-pVTZ, UCCSD(T)-F12a/aug-cc-pVTZ, UCCSD(T)-F12b/aug-cc-pVTZ and UCCSD(T)/aug-cc-pVQZ. By comparison, it is found that UCCSD(T)-F12/aug-cc-pVTZ provides practically the same results as UCCSD(T)-F12b/aug-cc-pVTZ and the agreement with UCCSD(T)/aug-cc-pVQZ is slightly better than UCCSD(T)-F12a/aug-cc-pVTZ. The largest energy difference between UCCSD(T)-F12/aug-cc-pVTZ (UCCSD(T)-F12b/aug-cc-pVTZ) and UCCSD(T)/aug-cc-pVQZ occurs for the transition state geometry, being 0.27 kcal mol⁻¹. In addition, the energy discrepancy between UCCSD(T)/aug-cc-pVTZ and UCCSD(T)/aug-cc-pVQZ is relatively larger, about 0.5 kcal mol⁻¹ for all stationary points. Since the single point energy calculation by UCCSD(T)-F12/aug-cc-pVTZ is about 10% faster than by UCCSD(T)-F12b/aug-cc-pVTZ for the stationary points, the energies of all sampled points are calculated at the level of UCCSD(T)-F12/aug-cc-pVTZ,^{21,22} implemented by the software MOLPRO 2012.²³

The first batch of data points are sampled by Atom Centered Density Matrix Propagation (ADMP) molecular dynamics, which is performed by Gaussian 09, Revision E.01²⁴ at the level of B3LYP/6-311G*. These points selected from the ADMP trajectories are used to generate a raw PES. Starting from the raw PES, batches of QCT trajectories are launched from

different initial conditions. New points whose geometries are not close to the existing data set are selected and added to the data set to patch up the unphysical regions of the PES. The closeness between two points $\{\vec{r}_i\}$ and $\{\vec{r}_i'\}$ is judged by the

Euclidean distance, which is defined as $\chi = \sqrt{\sum_{i=1}^{10} |\vec{r}_i - \vec{r}_i'|^2}$. The

permutationally equivalent points are also included in such a screening. The points that satisfy $\chi > 0.08$ Å in the interaction region or $\chi > 0.2$ Å in the asymptotic region are retained. This procedure is repeated dozens of times, like the GROW procedure suggested by Collins.²⁵ A new PES, usually better than the last one, is generated every time when a new batch of points are added to the data set. At last, there are totally 41 282 points in the data set with an energy interval of 105 kcal mol⁻¹.

The PES is fitted by the fundamental-invariant neural network (FI-NN) method,²⁶ which not only possesses the flexibility of the NN method, but also keeps the permutation invariance by introducing permutationally invariant polynomials (PIPs) to the NN as inputs.^{27,28} The NN fitting can approximate any function to arbitrary accuracy theoretically provided sufficient data points are sampled in the relevant configuration space.²⁹ The Morse-like variables, $P_{ij} = \exp(-r_{ij}/\alpha)$, are used to construct the monomials with α as an adjustable constant ($\alpha = 1.0$ Å in this work), in which r_{ij} is the internuclear distance between the *i*th and *j*th atoms.³⁰ The fits are actually insensitive to the precise value of α .³⁰ For the H_3NF system, there are 20 fundamental invariant polynomials with a maximum degree of 3. The architecture of the NN is 20-30-60-1, 20 invariant polynomials in the input layer, 30 and 60 neurons in the two hidden layers, and 1 potential energy in the output layer, producing totally 2551 parameters. All fittings are carried out using the Levenberg-Marquardt algorithm.^{29,31} The root mean square error (RMSE),

defined as $RMSE = \sqrt{\sum_{i=1}^{N_{data}} (E_{fit} - E_{ab initio})^2} / N_{data}$, is used as the

criterion to assess the quality of each fitting. The data set is randomly divided into two groups, 95% of the points as the training set and the rest 5% as the validating set. The fits with the two sets having small and close RMSEs are considered to be reasonable. In addition to the RMSE, the smoothness of the PES along different dimensions, the properties of the stationary points and the minimum energy path and the energy conservation in the QCT propagation are all used to assess to quality of the fitting. Finally, the so-called ensemble approach is implemented to minimize random errors.³² The final PES by averaging four best fits has a RMSE of 0.13 kcal mol⁻¹.

III. Quasi-classical trajectory method

The QCT method is well implemented in the software VENUS 96.³³ By interfacing the newly developed FI-NN PES with the software, the integral cross section (ICS) of the reaction is computed according to

$$\sigma_r(E_c) = \pi b_{\max}^2 P_r(E_c), \quad (1)$$

where $P_r(E_c)$ is the reaction probability defined as the ratio between the number of the reactive trajectories N_r and total trajectories N_{tot} at a specified collision energy E_c . b_{max} is the maximum impact parameter, which is determined using small batches of trajectories with trial values at each specified initial state and each collision energy. The relative statistical error is given by $\Delta = \sqrt{(N_{\text{tot}} - N_r)/N_{\text{tot}}N_r}$.

The DCS is calculated by

$$\frac{d\sigma_r}{d\Omega} = \frac{\sigma_r P_r(\theta)}{2\pi \sin(\theta)}, \quad (2)$$

where $P_r(\theta)$ is the normalized probability with the scattering angle θ defined as

$$\theta = \cos^{-1} \left(\frac{\vec{v}_i \cdot \vec{v}_f}{|\vec{v}_i||\vec{v}_f|} \right), \quad (3)$$

in which $\vec{v}_i = \vec{v}_F - \vec{v}_{\text{NH}_3}$ and $\vec{v}_f = \vec{v}_{\text{HF}} - \vec{v}_{\text{NH}_2}$. In practice, the scattering angle θ from 0 to 180° is evenly divided by 20 parts. The trajectory with the scattering angle located within the range of $\theta' \pm 4.5^\circ$ is attributed to θ' , $\theta' = 4.5^\circ, 13.5^\circ, \dots, 175.5^\circ$. $P_r(\theta')$ is calculated by

$$P_r(\theta') = \frac{\sum_{\theta \in \theta' \pm 4.5} N_r(\theta)}{N_r}. \quad (4)$$

The rate coefficient at temperature T is obtained by

$$k(T) = \frac{1}{Q_e} \left(\frac{8k_B T}{\pi\mu} \right)^{1/2} \pi b_{\text{max}}^2 \frac{N_r}{N_{\text{tot}}}, \quad (5)$$

where μ is the reduced mass between the reactants F and NH_3 and k_B is the Boltzmann constant. The electronic partition function Q_e is obtained by $(4 + 2e^{-404/k_B T})/2$, given that the spin-orbit splitting of F is 404 cm^{-1} .³⁴ At each specific temperature T , the collision energy and the initial ro-vibrational energies of the two reactants are both sampled according to the Boltzmann distribution.

The vibrational state of the product HF is determined by the Einstein–Brillouin–Keller semiclassical quantization of the action integral.³⁵ In contrast, the vibrational quantization for polyatomic molecules is not straightforward. In this work, the normal mode analysis (NMA) method^{36–39} is employed to calculate the vibrational state distribution of NH_2 . Traditionally, the coordinates and momenta required in the NMA calculations are taken from the last step of each trajectory, as has been done by Corchado and Espinosa-García.^{36–38} In this work, the coordinates and momenta are extracted from a specific step of each trajectory within the last vibrational period of the product molecules.^{12,40,41} This step is determined on the condition that the corresponding geometry has the lowest potential energy within the vibrational period, guaranteeing, at least to some extent, the accurate of the harmonic approximation inherent in the NMA method. Two binning methods, namely histogram binning (HB)⁴² and energy-based Gaussian binning (1GB),^{39,43,44} are implemented in the calculations.

In dynamics calculations, the reactant NH_3 is set on the ground ro-vibrational state. When compared with experimental results, the collision energy is taken at 4.5 kcal mol^{-1} and the ro-vibrational states are sampled at 20 K according to the Boltzmann distribution. The trajectories are initiated from a reactant separation of 8.0 Å and ended when products or reactants reach a separation of 8.0 Å for reactive or non-reactive trajectories. The time step is taken as 0.01 fs, which conserves the energy better than 10^{-4} kcal mol^{-1} in the propagation. 80 000–200 000 trajectories are launched from each initial state, which keeps the relative statistical errors all below 0.5%.

IV. Results and discussion

A. Properties of potential energy surface

Fig. 1 shows the schematic diagram of the reaction path for the $\text{F} + \text{NH}_3 \rightarrow \text{HF} + \text{NH}_2$ reaction. The *ab initio* energy at the level of UCCSD(T)-F12/aug-cc-pVTZ, the fitted potential energy and the zero-point energy (ZPE) corrected energy of each stationary points along the reaction path are listed in the figure as well. Clearly, there exists a submerged transition state with C_s symmetry, flanked by two minima in the entrance and exit valleys. The pre-reaction $\text{NH}_3 \cdots \text{F}$ complex has a tetrahedral structure with C_{3v} symmetry while the post-reaction $\text{NH}_2 \cdots \text{HF}$ complex presents a planar structure with C_{2v} symmetry. The $\text{NH}_2 \cdots \text{HF}$ complex appears to be the global minimum, having a depth of 9.968 kcal mol^{-1} (10.034 kcal mol^{-1} in the fitted PES) with respect to the product asymptote. It is very close to Feng *et al.*'s result of 9.93 kcal mol^{-1} at the level of CCSD(T)/aug-cc-pVQZ by the CFOUR program package.⁴ It is note in passing that two other stationary geometries have been determined by Xiao *et al.*¹⁷ at the level of UCCSD(T)/aug-cc-pVTZ, however,

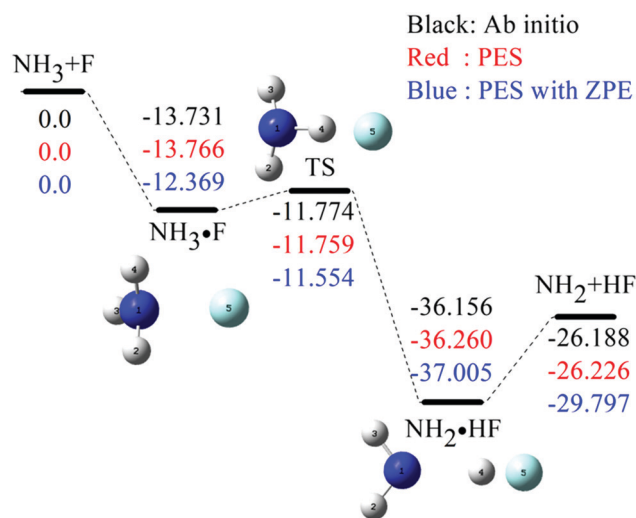


Fig. 1 Schematic diagram of the reaction path for the $\text{F} + \text{NH}_3 \rightarrow \text{HF} + \text{NH}_2$ reaction. The *ab initio* energies of stationary points at the level of UCCSD(T)-F12/aug-cc-pVTZ (black), the values of the fitted PES (red) and the zero-point energy corrected values (blue) are shown below the corresponding geometries. All energies are given in kcal mol^{-1} and relative to the reactant asymptote.

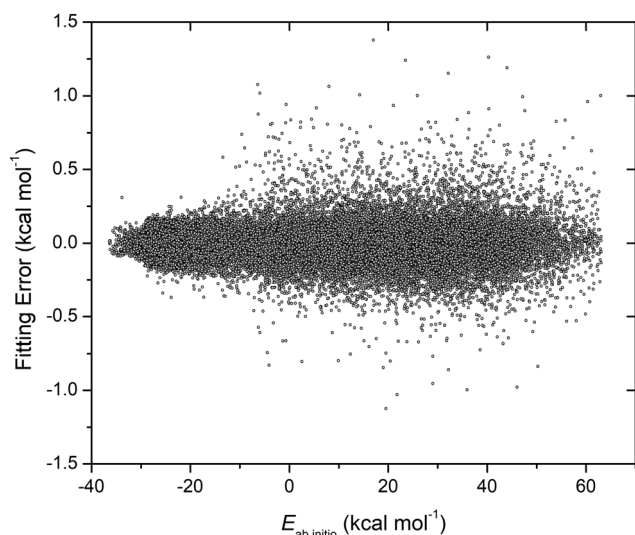


Fig. 2 Fitting errors ($E_{\text{fit}} - E_{\text{ab initio}}$) as a function of energy.

they cannot be obtained by optimization at the level of UCCSD(T)-F12/aug-cc-pVTZ and UCCSD(T)/aug-cc-pVQZ. Fig. 2 shows the fitting errors of the sampled data points as a function of energy. It can be seen that the fitting errors are almost evenly distributed within the range of ± 1.4 kcal mol $^{-1}$

over the whole energy range studied, indicating a good flexibility of the neural network method.

The optimized geometries of the stationary points at the level of UCCSD(T)-F12/aug-cc-pVTZ and on the fitted PES are given in Table 1, together with Espinosa-García *et al.*'s results on PES-1997,¹⁸ Feng *et al.*'s results at the level of CCSD(T)/aug-cc-pVQZ⁴ and available experimental values⁴⁵ for comparison. It can be seen that, on one hand, the optimized geometries at the level of UCCSD(T)-F12/aug-cc-pVTZ agree well with those at the level of CCSD(T)/aug-cc-pVQZ. The bond length difference is less than 0.006 Å and the angle difference is smaller than 0.23°. On the other hand, the fitted geometries reproduce well the *ab initio* data at the level of CCSD(T)/aug-cc-pVQZ, in which the bond lengths differ by less than 0.015 Å and the angles differ by less than 2.96°. In addition, the fitted geometries are also in good accord with the experimental values. Table 2 lists the corresponding energies and harmonic frequencies of the stationary points. Again, the fitted values, no matter energies and harmonic frequencies, are in good agreement with the *ab initio* calculations by UCCSD(T)-F12/aug-cc-pVTZ (or CCSD(T)/aug-cc-pVQZ) as the energy difference is less than 0.116 (0.144) kcal mol $^{-1}$ and the frequency difference is mostly less than 20 (30) cm $^{-1}$.

Fig. 3 displays the contours of the PES as a function of bond lengths of the breaking bond N–H and the forming bond H–F

Table 1 Geometries (bond length in angstrom and angle in degree) of the stationary points for the $\text{F} + \text{NH}_3 \rightarrow \text{HF} + \text{NH}_2$ reaction. The corresponding atom labels are shown in Fig. 1

Species	Method	R_{N1H2}	R_{N1H3}	R_{N1F4}	R_{H4F5}	θ_{H2N1H3}	θ_{H2N1H4}	θ_{H2H4F5}	ϕ_{H3H2N1H4}	ϕ_{H3H2H4F5}
NH ₃	<i>Ab initio</i> ^a	1.012	1.012	1.012		106.62	106.62		−113.62	
	PES ^b	1.013	1.013	1.013		106.57	106.57		−113.52	
	<i>Ab initio</i> ^c	1.013	1.013	1.013		106.5	106.5			
	PES ^d	1.012	1.012	1.012		106.7	106.7			
	Expt. ^e	1.012	1.012	1.012		106.7	106.7			
NH ₃ ·F	<i>Ab initio</i> ^a	1.005	1.005	1.005	2.371	115.53	115.53	69.00	139.24	−77.19
	PES ^b	1.005	1.005	1.005	2.386	114.80	114.80	69.21	136.28	−77.34
	<i>Ab initio</i> ^c	1.005	1.005	1.005		115.3	115.3			
TS	<i>Ab initio</i> ^a	1.011	1.011	1.043	1.500	112.34	112.24	94.23	−127.60	−92.40
	PES ^b	1.011	1.011	1.040	1.515	112.71	112.20	94.03	−127.82	−92.30
	<i>Ab initio</i> ^c	1.011	1.011	1.042	1.500	112.2	112.1			
NH ₂ ·HF	<i>Ab initio</i> ^a	1.021	1.021	1.759	0.938	105.59	127.21	161.10	−180.0	−180.0
	PES ^b	1.021	1.021	1.752	0.939	105.73	127.13	161.03	−180.0	−180.0
	<i>Ab initio</i> ^c	1.022	1.022	1.757	0.939	105.5	127.25		−180.0	−180.0
	PES ^d	1.013	1.013	1.409	0.927	105.7	108.7	175.8		
	Expt. ^e	1.021	1.774		0.929	105.2			−180.0	
NH ₂	<i>Ab initio</i> ^a	1.025	1.025			103.03				
	PES ^b	1.025	1.025			103.04				
	<i>Ab initio</i> ^c	1.025	1.025			103.0				
	PES ^d	1.012	1.012			103.4				
	Expt. ^e	1.024	1.024			103.4				
HF	<i>Ab initio</i> ^a				0.918					
	PES ^b				0.918					
	<i>Ab initio</i> ^c				0.918					
	PES ^d				0.917					
	Expt. ^e				0.917					

^a This work, UCCSD(T)-F12/aug-cc-pVTZ by Molpro 2010. ^b This work, FI-NN PES. ^c CCSD(T)/aug-cc-pVQZ by CFOUR, see ref. 4. ^d PES-1997, see ref. 18. ^e See ref. 45.

Table 2 Energies (in kcal mol⁻¹) and harmonic frequencies (in cm⁻¹) of the stationary points for the F + NH₃ → HF + NH₂ reaction

Species	Method	<i>E</i> (kcal mol ⁻¹)	Frequency (cm ⁻¹)								
			1	2	3	4	5	6	7	8	9
F + NH ₃	<i>Ab initio</i> ^a	0.0	3609	3609	3478	1674	1673	1055			
	PES ^b	0.0	3611	3611	3483	1674	1674	1063			
	<i>Ab initio</i> ^c	0.0	3593	3593	3464	1673	1673	1063			
	PES ^d	0.0	3542	3542	3433	1072	1072	999			
	Expt. ^e	0.0	3577	3577	3506	1691	1691	1022			
NH ₃ ·F	<i>Ab initio</i> ^a	-13.73	3732	3732	3545	1618	1618	636	457	349	349
	PES ^b	-13.77	3721	3721	3564	1614	1614	727	468	342	342
	<i>Ab initio</i> ^c	-13.67	3711	3711	3530	1624	1624	684	450	341	341
	PES ^d	-6.11									
TS	<i>Ab initio</i> ^a	-11.77	3665	3564	3072	1611	1537	780	482	455	543i
	PES ^b	-11.76	3657	3569	3106	1606	1555	834	506	448	524i
	<i>Ab initio</i> ^c	-11.63	3651	3550	3066	1615	1539	785	487	452	554i
NH ₂ ·HF	<i>Ab initio</i> ^a	-36.16	3681	3522	3422	1544	834	795	301	247	211
	PES ^b	-36.26	3674	3522	3425	1555	844	829	318	251	197
	<i>Ab initio</i> ^c	-36.20	3670	3506	3408	1544	832	800	303	246	213
	PES ^d	-32.05	3771	3397	3338	1610	978	806	230	214	195
HF + NH ₂	<i>Ab initio</i> ^a	-26.19	4143	3471	3376	1542					
	PES ^b	-26.23	4152	3482	3385	1555					
	<i>Ab initio</i> ^c	-26.27	4125	3454	3360	1540					
	PES ^d	-25.80	4140	3205	3164	1508					
	Expt. ^e	-28.14	4139	3220	3173	1497					

^a This work, UCCSD(T)-F12/aug-cc-pVTZ by Molpro 2010. ^b This work, FI-NN PES. ^c CCSD(T)/aug-cc-pVQZ by CFOUR, see ref. 4. ^d PES-1997, see ref. 18 and 20. ^e See ref. 45.

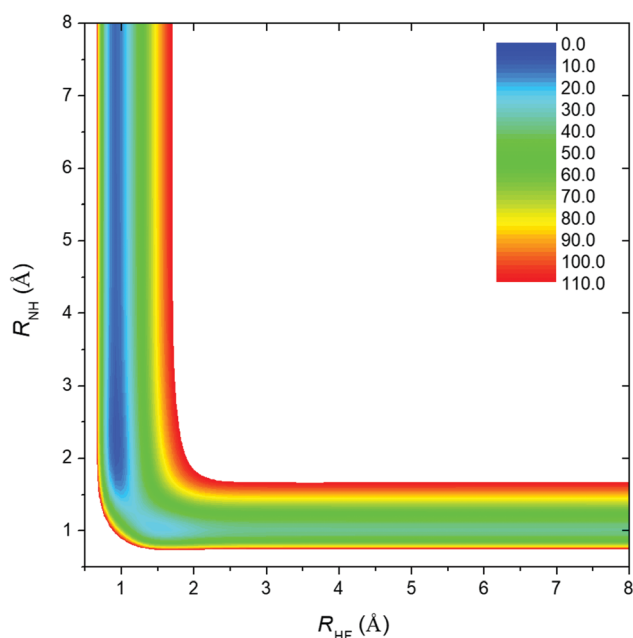


Fig. 3 Contours of the PES as a function of bond lengths of the breaking bond N–H and the forming bond H–F with the other internal coordinates fixed at the geometry of the transition state. The energy range of energies is taken from 0 to 110 kcal mol⁻¹ with an interval of 2 kcal mol⁻¹.

with the other internal coordinates fixed at the transition state geometry. Obviously, the fitted PES is very smooth. The pre- and post-reaction wells and the submerged barrier are immediately

seen. By plotting the contours along different dimensions, the existence of any artificial wells on the PES is excluded. The minimum energy path (MEP) along the reaction coordinate *s* and the associated vibrationally adiabatic ground state energy defined as $V_a^G(s) = V_{MEP}(s) + ZPE(s)$, as shown in Fig. 4(a), are determined on the PES using the software POLYRATE 9.7.⁴⁶ The reaction coordinate (*s*) is defined as the signed distance from the saddle point (*s* = 0), with *s* > 0 referring to the product side and *s* < 0 to the reactant side. The *ab initio* values at the level of UCCSD(T)-F12/aug-cc-pVTZ along the minimum energy path are also given for comparison. The good agreement between the fitted and *ab initio* MEPs indicates the good quality of the PES. In addition, a generalized normal-mode analysis along the reaction coordinate is performed using the redundant curvilinear projection formalism. The obtained normal mode vibrational frequencies are shown in Fig. 4(b). The vibrational frequency of each mode varies smoothly along the reaction coordinate *s*.

B. Dynamics

The calculated integral cross sections (ICSs) of the F + NH₃ → HF + NH₂ reaction from the reactant ground ro-vibrational state are plotted in Fig. 5(a) as a function of collision energy. The ICS first decreases monotonically with the increase of collision energy, then starts to increase slowly, and finally becomes more or less flat. The rapid decrease of the ICS at low collision energies satisfies the nature of barrierless reactions. The corresponding DCSs are shown in Fig. 5(b), for which the collision energy is fixed at 4.5, 10.0, 15.0, 23.0 and 27.0 kcal mol⁻¹.

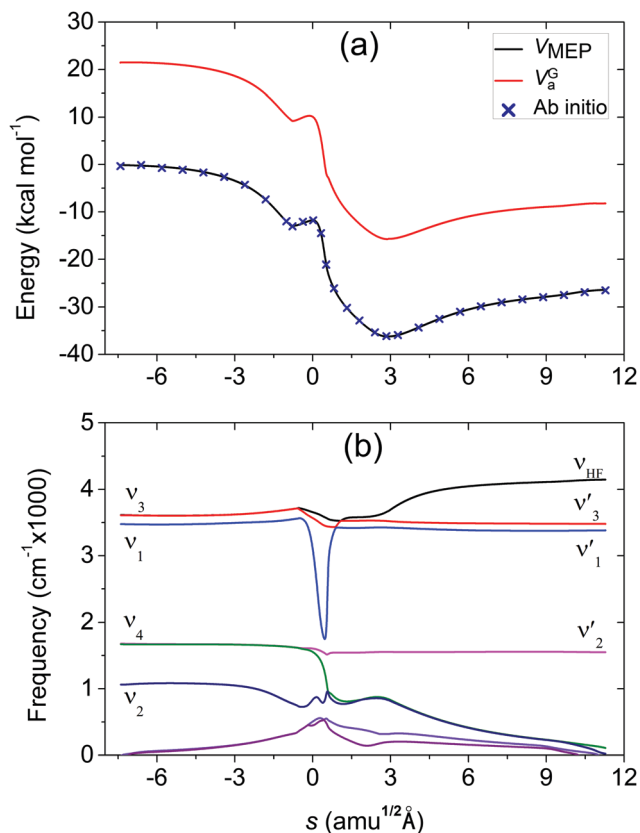


Fig. 4 (a) Minimum energy path, V_{MEP} , and vibrationally adiabatic ground state energy, V_a^G , as a function of the reaction coordinate s . *Ab initio* energies at the level of UCCSD(T)-F12/aug-cc-pVTZ along the minimum energy path are also given for comparison; (b) generalized normal mode vibrational frequencies as a function of s . ν_1 , ν_2 , ν_3 and ν_4 denote the vibrational frequencies of the symmetric stretching mode, the umbrella mode, the asymmetric stretching mode and the asymmetric bending mode of NH_3 , respectively, while ν'_1 , ν'_2 and ν'_3 refer to the symmetric stretching mode, the bending mode and the asymmetric stretching mode of NH_2 , respectively. The energy is given relative to the reactant asymptote.

It can be seen that the reaction is dominated by the forward scattering while the sideways and backward scattering is nonnegligible. The contribution of the backward scattering decreases as the collision energy increases. Xiao *et al.* measured the product angular distribution at $E_c = 4.5 \text{ kcal mol}^{-1}$ using the crossed beams technique. The product angular distribution of HF, as shown in Fig. 5b, is largely forward-scattered with a considerable amount of product at sideways and backward scattering directions.¹⁷ Therefore, the calculated DCS is reasonably consistent with the experimental result.

In order to understand the reaction mechanism associated with different scattering directions, the scattering angle is correlated with the impact parameter at different collision energies, as shown in Fig. 6. The reaction with large impact parameter and small scattering angle along the diagonal line corresponds to the direct stripping mechanism. On the other side, the reaction with small impact parameter and large scattering angle refers to the direct rebound mechanism.

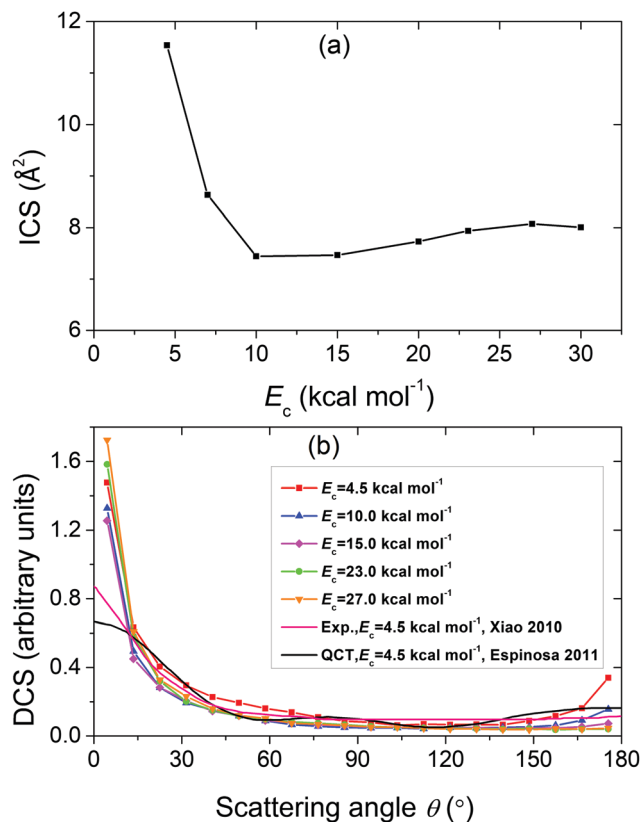


Fig. 5 (a) Integral cross sections of the $\text{F} + \text{NH}_3 \rightarrow \text{HF} + \text{NH}_2$ reaction from the ground state of NH_3 as a function of collision energy; (b) the corresponding differential cross sections with the collision energy E_c fixed at 4.5, 10.0, 15.0, 23.0 and 27.0 kcal mol^{-1} , respectively, together with Xiao *et al.*'s experimental result¹⁷ and Espinosa-García *et al.*'s theoretical result.¹⁹

In addition, the reaction with large impact parameter in between 2.0 and 3.5 \AA and scattering angle spanning the whole range from 0 to 180° is attributed to the indirect mechanism. The reactive trajectories are analyzed at $E_c = 4.5 \text{ kcal mol}^{-1}$. It is found that about 67% of the trajectories are direct while the rest 33% are indirect. The number of the indirect trajectory is roughly obtained by counting the trajectories for which either the forming bond HF or the breaking bond NH has large-amplitude vibrations (about 0.5–1.5 \AA) for more than one period, while the rest of reactive trajectories is considered to be direct. Thus, the reaction is dominated by the direct mechanism while the indirect mechanism makes a visible contribution. The contribution of the indirect mechanism decreases as the collision energy increases. In addition, as aforementioned, the ICS slightly increases with the collision energy from 15 to 27 kcal mol^{-1} . It can be seen from Fig. 5(b) that, as the collision energy increases, the backward scattering is slightly depressed while the forward scattering is visibly enhanced. As the forward scattering mainly results from the direct stripping mechanism, the increase of the cross section is caused by the enhancement of the direct stripping mechanism.

Espinosa-García and Monge-Palacios also observed indirect trajectories in their QCT calculations on the PES-1997.¹⁹

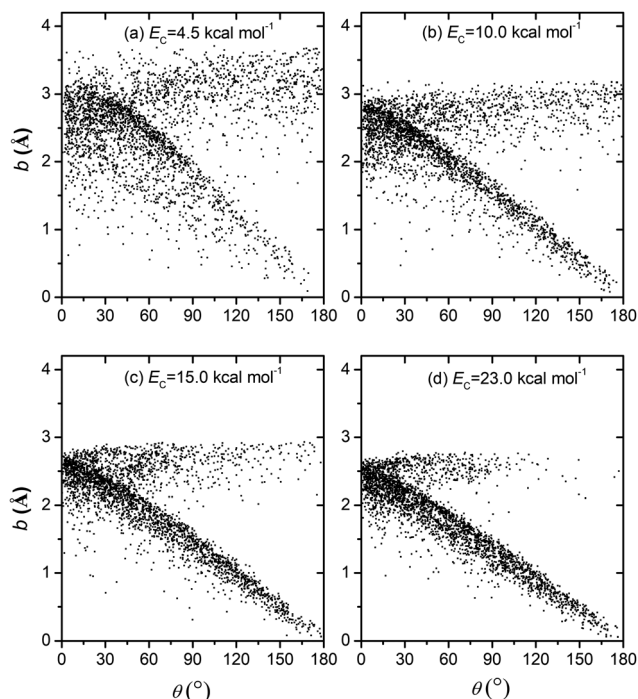


Fig. 6 Correlation between the impact parameter b and the scattering angle at $E_c = 4.5, 10.0, 15.0$ and 23.0 kcal mol $^{-1}$.

They argued that the indirect trajectories are not originated from long-lived complexes caused by the presence of the deep post-reaction well. Instead, these “nearly-trapped” trajectories are more like the motion of a spring or a “yo-yo” since the colliders undergo several collisions before separating. It is clearly seen from Fig. 5 that the indirect trajectories are almost exclusively generated from large impact parameters, rather than from relatively small impact parameters usually observed in the complex-forming mechanism, thus supporting the “yo-yo” mechanism. The indirect reactive trajectories at $E_c = 4.5$ kcal mol $^{-1}$ are further analyzed to clarify the origins. The indirect trajectories with the forming bond HF having large-amplitude vibrations are attributed to the reactant well while the rest with the breaking NH having large-amplitude vibrations are referred to the product well. Roughly, about 85% of the trajectories are caused by the shallow reactant well while 15% of them result from the deep product well. In contrast, Espinosa-García and Monge-Palacios attributed the indirect trajectories to the existence of the product well.¹⁹ The discrepancy is possibly caused by the inaccurate description of the reactant well and the submerged barrier on the PES-1997.

Fig. 7 shows the product energy partitioning for the $F + NH_3 \rightarrow HF + NH_2$ reaction at $E_c = 4.5$ kcal mol $^{-1}$. $f_v(NH_2)$, $f_r(NH_2)$, $f_v(HF)$, $f_r(HF)$ and f_{trans} denote the fractions of the available energy released as the vibrational energy of NH_2 , the rotational energy of NH_2 , the vibrational energy of HF, the rotational energy of HF and the product translational energy. As can be seen from the figure, the available energy is largely transferred into the vibrational energy of HF, followed by the product translational energy and the vibrational energy

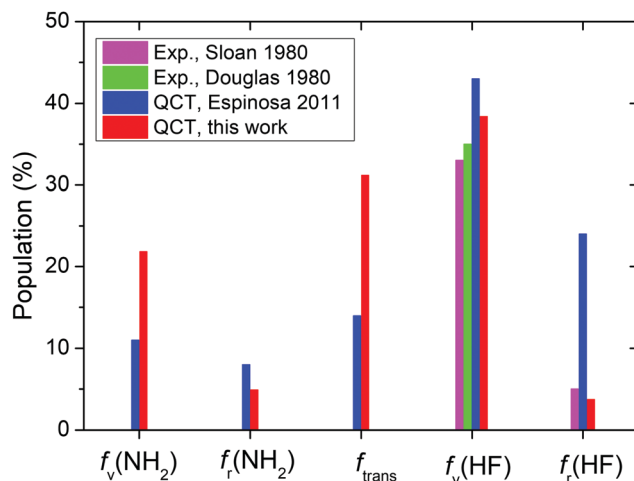


Fig. 7 Product energy disposal for $F + NH_3 \rightarrow HF + NH_2$ reaction at $E_c = 4.5$ kcal mol $^{-1}$. The initial ro-vibrational energy of the reactant NH_3 is sampled at 20 K according to the Boltzmann distribution in order to compare with the experimental results.

of NH_2 . It appears that the energy cannot effectively flow into the rotational modes of both products. The bias to the product vibrational modes is easily understood considering the geometry change from the TS to the products. For the product HF, the bond distance is shortened from 1.5 Å to 0.918 Å. For the product NH_2 , although the bond distances of the two NH bonds don't change too much, the bending angle varies from 112.34° to 103.03°, indicating that the bending mode will be excited in the reaction. Furthermore, as aforementioned, the reaction is dominated by the direct mechanism, in favor of the available energy flowing into the product translational motion.

The calculated product energy partitioning is also compared with previous theoretical result on the PES-1997¹⁹ and available experimental values^{47,48} in Fig. 7. The fractions of the energy in vibration and rotation of the product HF agree well with the experimental values. In contrast, Espinosa-García and Monge-Palacios overestimated the percentage of the rotational energy of HF on the PES-1997 while the percentage of the vibrational energy is reasonably duplicated. They attributed the overestimation to an excessively attractive character of the stretching terms of the function form describing the PES-1997.

The vibrational state distribution of the product HF in the $F + NH_3 \rightarrow HF + NH_2$ reaction has been debated in the past several decades.³ In this work, the vibrational distributions of the products HF and NH_2 are calculated as well, as shown in Fig. 8. Both HB and GB methods give similar vibrational state distributions. The product HF is mainly populated in the $\nu_{HF} = 1$ and $\nu_{HF} = 2$ states, followed by the ground states and the $\nu_{HF} = 3$ state. The product NH_2 is largely populated in the ground state, followed by the fundamental excitation of the bending mode. The distributions are expected from the geometry changes along the MEP. However, the vibrational state distribution of HF does not follow any of the scattered experimental results,^{2,13,14} as shown in Fig. 8a. Note that it is impossible to determine the $\nu_{HF} = 0$ population in these

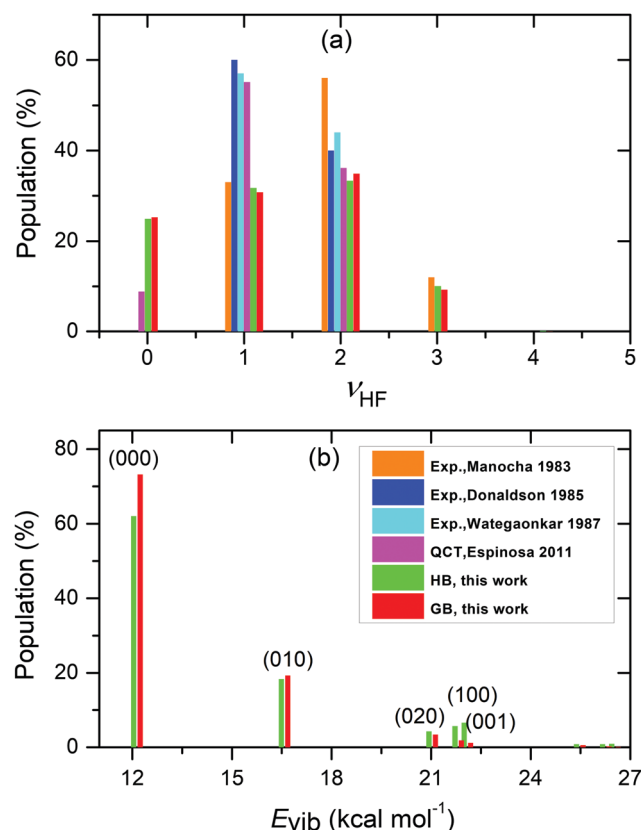


Fig. 8 Vibrational state distributions of (a) HF and (b) NH_2 for the $\text{F} + \text{NH}_3 \rightarrow \text{HF} + \text{NH}_2$ reaction at $E_c = 4.5 \text{ kcal mol}^{-1}$. The initial ro-vibrational energy of the reactant NH_3 is sampled at 20 K according to the Boltzmann distribution in order to compare with the experimental results.

experiments.³ In our calculations, the population in the $\nu_{\text{HF}} = 1$ state is close to in the $\nu_{\text{HF}} = 2$ state. In contrast, the experiments presented either a vibrationally cold distribution with $P(\nu_{\text{HF}} = 1) > P(\nu_{\text{HF}} = 2)$ or a vibrationally inverted distribution. As the experimental conditions are not clear, QCT calculations from different initial conditions are performed on the FI-NN PES. It is found that the vibrational distribution of HF is not sensitive to the initial condition. All of the different initial conditions provide similar populations in the $\nu_{\text{HF}} = 1$ and $\nu_{\text{HF}} = 2$ state and the population in each of the two states is higher than in the ground state.

The state distributions are also inconsistent with Espinosa-García and Monge-Palacios's theoretical calculations,¹⁹ as shown in Fig. 8a, in which they found that the population in $\nu_{\text{HF}} = 1$ is higher than in $\nu_{\text{HF}} = 2$ and they both are much larger than in $\nu_{\text{HF}} = 0$. The discrepancy is, on one hand, possibly caused by the different topologies of the PESs around the submerged transition state. On the other hand, we do not deal with the ZPE problem in the QCT calculations, since there are actually no satisfactory methodologies until now. In Espinosa-García and Monge-Palacios's work, they discarded all the trajectories for which either of the products has a vibrational energy lower than the corresponding harmonic ZPE, which perturbs the statistics in dynamics calculations. In addition,

the spin-orbital coupling effect of the atom F and the non-adiabatic coupling are not considered in both of two PESs. Therefore, more work would be needed to settle the controversy associated with the vibrational state distribution of HF.

C. Kinetics

The thermal rate coefficients of the $\text{F} + \text{NH}_3 \rightarrow \text{HF} + \text{NH}$ have been measured by Persky's¹⁶ and Walther and Wagner's groups.¹⁵ However, different temperature dependences were reported at low temperature. The calculated rate constants on the FI-NN PES are listed in Table 3 and displayed in Fig. 9, together with the TST, QCT and RPMD results on the PES-1997^{18,20} and available experimental results.^{15,16} Fig. 9a shows a detailed comparison of the rate constants in the temperature range of 270–330 K. The calculated rate constants on the FI-NN PES are actually independent of temperature and located within the experimental uncertainties of Walther and Wagner. Espinosa-García *et al.*'s calculations on the PES-1997 by the TST, RPMD and QCT methods also show a very weak temperature.²⁰ In contrast, Persky's recent experiment displays a negative temperature dependence from 276 K to 327 K.¹⁶ Espinosa-García *et al.* made a detailed analysis to understand the difference with Persky's experiment. They argued that the negative temperature dependence was not observed in similar fast reactions, such as $\text{OH} + \text{OH}$ reaction, $\text{CH}_3 + \text{OH}$ reaction, ClO self-reaction and $\text{OH} + \text{CO}$ reaction, and the effect of the secondary reaction cannot be eliminated in the experiment.²⁰ In addition, as aforementioned, both of the two PESs, PES-1997 and FI-NN PES, did not consider the spin-orbital coupling effect of the atom F.

As can be seen from Fig. 9a, the rate constants calculated by Espinosa-García *et al.*^{18,20} are visibly larger than ours. The difference possibly results from the effect of the reactant complex, which is reported to be $-6.11 \text{ kcal mol}^{-1}$ with respect to the reactants on the PES-1997, in sharp contrast to the value of $-13.77 \text{ kcal mol}^{-1}$ on the FI-NN PES. On the other hand, there exists a submerged barrier on the FI-NN PESs, which is also likely to affect the reaction dynamics.

Table 3 Thermal rate coefficients ($\times 10^{-10} \text{ cm}^3 \text{ molecule}^{-1} \text{ s}^{-1}$) for the $\text{F} + \text{NH}_3 \rightarrow \text{HF} + \text{NH}_2$ reaction

T (K)	QCT ^a	Exp. ^b	Exp. ^c
200	1.176		0.097 ± 2.778
250	1.203		0.185 ± 2.390
276	1.258	3.6 ± 0.45	0.237 ± 2.259
278	1.202	2.70 ± 0.30	0.241 ± 2.250
283	1.185	1.95 ± 0.22	0.251 ± 2.228
290	1.209	1.37 ± 0.12	0.265 ± 2.200
292	1.212	1.15 ± 0.12	0.269 ± 2.192
298	1.201	$1.03 \pm 0.12/$ 1.0 ± 0.08	0.282 ± 2.170
300	1.219		0.286 ± 2.162
327	1.208	0.91 ± 0.10	0.342 ± 2.075
369	1.211		0.428 ± 1.969
500	1.231		0.679 ± 1.770
1000	1.277		1.301 ± 1.523
1500	1.489		1.615 ± 1.448

^a QCT, this work. ^b Exp., Persky 2007, see ref. 16. ^c Exp., Walther 1983, see ref. 15.

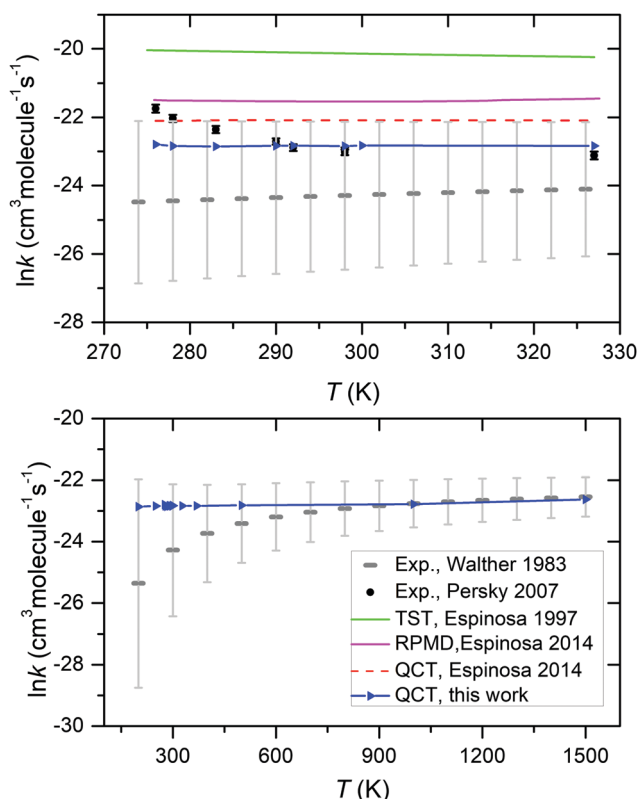


Fig. 9 Comparison of the calculated and measured thermal rate constants for the $\text{F} + \text{NH}_3 \rightarrow \text{HF} + \text{NH}_2$ reaction.

Fig. 9b shows the rate constants in the temperature range of 100–1600 K. The rate constants on the FI-NN PES presents no temperature dependence over the temperature range studied. At low temperatures below 900 K, the experimental rate constants by Walther *et al.* display, however, a positive temperature dependence although the experimental uncertainty is very large.¹⁵ As the temperature increases, the agreement between theoretical and experimental results becomes better. The nearly constant value of the rate coefficient in the whole range of temperature calculated on the FI-NN PES can be understood by the underlying reaction mechanism. At low temperatures (or low collision energies), the indirect mechanism is favored. The large cone of acceptance of the indirect mechanism results in high reactivity. With the increase of the temperature, the direct mechanism becomes more preferred and the cone of acceptance becomes narrower. As the quantum tunneling effect is neglect in this work, theoretical studies based on more accurate methods, such as RPMD, are desired.

V. Conclusions

In this work, we report an accurate full-dimensional *ab initio* PES for the $\text{F} + \text{NH}_3 \rightarrow \text{HF} + \text{NH}_2$ reaction. The fundamental-invariant neural network method is utilized to fit the PES based on 41 282 *ab initio* energy points sampled in the relevant configurational space at the level of UCCSD(T)-F12/aug-cc-pVTZ,

resulting in a total RMSE of $0.13 \text{ kcal mol}^{-1}$. The geometries, energies and harmonic frequencies of the stationary points along the MEP are all well reproduced by the PES. The Fortran subroutine of the PES is provided in the ESI.†

The QCT method is then employed to study the dynamics and kinetics of the reaction on the newly developed PES. The reaction is dominated by the forward scattering while the sideways and backward scattering is nonnegligible, reasonably consistent with Xiao *et al.*'s crossed beams experiment. By correlating the scattering angle with the impact parameter, it is found that the reaction takes place mainly through the direct rebound and stripping mechanisms. The indirect “yo-yo” mechanism, by which a considerable amount of reaction occurs, results largely from the presence of the well in the entrance valley. In addition, the calculated product energy partition agrees well with available experimental results, which can be rationalized by considering the geometry change along the MEP. The obtained vibrational state distribution of the product HF, *i.e.* $P_{\nu_{\text{HF}}=2} \approx P_{\nu_{\text{HF}}=1} > P_{\nu_{\text{HF}}=0} > P_{\nu_{\text{HF}}=3}$, is insensitive to the initial conditions but in sharp contrast to the scattered experimental results. The discrepancy between the theoretical and experimental vibrational-state distribution is possibly caused by the neglect of the spin-orbital coupling effect of the atom F and the nonadiabatic coupling for the PES. In addition, the calculated thermal rate coefficients that are well located within the experimental uncertainties of Walther and Wagner show practically no temperature dependence within the statistical errors.

Conflicts of interest

There are no conflicts to declare.

Acknowledgements

This work is supported by the National Natural Science Foundation of China (Grant No. 21603266 to HS and 21773297 to MY).

References

- 1 D. J. Donaldson, J. Parsons, J. J. Sloan and A. Stolow, *Chem. Phys.*, 1984, **85**, 47–62.
- 2 D. J. Donaldson, J. J. Sloan and J. D. Goddard, *J. Chem. Phys.*, 1985, **82**, 4524–4536.
- 3 J. D. Goddard, D. J. Donaldson and J. J. Sloan, *Chem. Phys.*, 1987, **114**, 321–329.
- 4 H. Feng, W. Sun, Y. Xie and H. F. Schaefer, *Chem. – Asian J.*, 2011, **6**, 3152–3156.
- 5 B. A. Ellingson and D. G. Truhlar, *J. Am. Chem. Soc.*, 2007, **129**, 12765–12771.
- 6 P. Manikandan, J. Zhang and W. L. Hase, *J. Phys. Chem. A*, 2012, **116**, 3061–3080.
- 7 I. Szabó, A. G. Császár and G. Czako, *Chem. Sci.*, 2013, **4**, 4362.

- 8 A. G. S. de Oliveira-Filho, F. R. Ornellas and J. M. Bowman, *J. Phys. Chem. Lett.*, 2014, **5**, 706–712.
- 9 H. Song, A. Li and H. Guo, *J. Phys. Chem. A*, 2016, **120**, 4742–4748.
- 10 H. Song, A. Li, H. Guo, Y. Xu, B. Xiong, Y. C. Chang and C. Y. Ng, *Phys. Chem. Chem. Phys.*, 2016, **18**, 22509–22515.
- 11 Y. Wang, H. Song, I. Szabó, G. Czako, H. Guo and M. Yang, *J. Phys. Chem. Lett.*, 2016, **7**, 3322–3327.
- 12 L. Ping, Y. Zhu, A. Li, H. Song, Y. Li and M. Yang, *Phys. Chem. Chem. Phys.*, 2018, **20**, 26315–26324.
- 13 A. S. Manocha, D. W. Setser and M. A. Wickramaaratchi, *Chem. Phys.*, 1983, **76**, 129–146.
- 14 S. Wategaonkar and D. W. Setser, *J. Chem. Phys.*, 1987, **86**, 4477–4487.
- 15 C. Walther and H. G. Wagner, *Ber. Bunsen-Ges.*, 1983, **87**, 403–409.
- 16 A. Persky, *Chem. Phys. Lett.*, 2007, **439**, 3–7.
- 17 C. Xiao, G. Shen, X. Wang, H. Fan and X. Yang, *J. Phys. Chem. A*, 2010, **114**, 4520–4523.
- 18 J. Espinosa-García and J. C. Corchado, *J. Phys. Chem. A*, 1997, **101**, 7336–7344.
- 19 J. Espinosa-García and M. Monge-Palacios, *J. Phys. Chem. A*, 2011, **115**, 13759–13763.
- 20 J. Espinosa-García, A. Fernandez-Ramos, Y. V. Suleimanov and J. C. Corchado, *J. Phys. Chem. A*, 2014, **118**, 554–560.
- 21 T. B. Adler, G. Knizia and H.-J. Werner, *J. Chem. Phys.*, 2007, **127**, 221106.
- 22 G. Knizia, T. B. Adler and H.-J. Werner, *J. Chem. Phys.*, 2009, **130**, 054104.
- 23 H.-J. Werner, P. J. Knowles, G. Knizia, F. R. Manby, M. Schütz, *et al.*, *MOLPRO, version 2012.1, a package of ab initio programs*, 2012, see <http://www.molpro.net>.
- 24 M. J. Frisch, G. W. Trucks, H. B. Schlegel, G. E. Scuseria, M. A. Robb, J. R. Cheeseman, G. Scalmani, V. Barone, G. A. Petersson, H. Nakatsuji, X. M. Li, *et al.*, *Gaussian 09, Revision B.01*, Gaussian, Inc., Wallingford CT, 2009.
- 25 M. A. Collins, *Theor. Chem. Acc.*, 2002, **108**, 313–324.
- 26 K. Shao, J. Chen, Z. Zhao and D. H. Zhang, *J. Chem. Phys.*, 2016, **145**, 071101.
- 27 B. Jiang and H. Guo, *J. Chem. Phys.*, 2013, **139**, 054112.
- 28 J. Li, B. Jiang and H. Guo, *J. Chem. Phys.*, 2013, **139**, 204103.
- 29 L. M. Raff, R. Komanduri, M. Hagan and S. T. S. Bukkapatnam, *Neural Networks in Chemical Reaction Dynamics*, Oxford University Press, Oxford, 2012.
- 30 Z. Xie and J. M. Bowman, *J. Chem. Theory Comput.*, 2009, **6**, 26–34.
- 31 M. T. Hagan and M. B. Menhaj, *IEEE Trans. Neural Networks*, 1994, **5**, 989–993.
- 32 Z.-H. Zhou, J. Wu and W. Tang, *Artif. Intell.*, 2002, **137**, 239–263.
- 33 W. L. Hase, R. J. Duchovic, X. Hu, A. Komornicki, K. F. Lim, D.-H. Lu, G. H. Peslherbe, K. N. Swamy, S. R. V. Linde, A. Varandas, H. Wang and R. J. Wolf, *Quantum Chem. Program Exch. Bull.*, 1996, **16**, 671.
- 34 T. L. Nguyen, J. Li, R. Dawes, J. F. Stanton and H. Guo, *J. Phys. Chem. A*, 2013, **117**, 8864–8872.
- 35 M. C. Gutzwiller, *Chaos in Classical and Quantum Mechanics*, Springer, New York, 1990.
- 36 J. Espinosa-García, J. L. Bravo and C. Rangel, *J. Phys. Chem. A*, 2007, **111**, 2761–2771.
- 37 J. Espinosa-García and J. L. Bravo, *J. Phys. Chem. A*, 2008, **112**, 6059–6065.
- 38 J. C. Corchado and J. Espinosa-García, *Phys. Chem. Chem. Phys.*, 2009, **11**, 10157–10164.
- 39 G. Czako and J. M. Bowman, *J. Chem. Phys.*, 2009, **131**, 244302.
- 40 L. Ping, L. Tian, H. Song and M. Yang, *J. Phys. Chem. A*, 2018, **122**, 6997–7005.
- 41 Y. Zhu, L. Ping, M. Bai, Y. Liu, H. Song, J. Li and M. Yang, *Phys. Chem. Chem. Phys.*, 2018, **20**, 12543–12556.
- 42 D. G. Truhlar and J. T. Muckerman, in *Atom-Molecule Collision Theory*, ed. R. B. Bernstein, Plenum, New York, 1979.
- 43 L. Bonnet and J.-C. Rayez, *Chem. Phys. Lett.*, 2004, **397**, 106–109.
- 44 L. Bonnet and J. Espinosa-García, *J. Chem. Phys.*, 2010, **133**, 164108.
- 45 M. W. Chase, Jr., C. A. Davies, J. R. Downey, Jr., D. J. Frurip, R. A. McDonald and A. N. Syverud, *J. Phys. Chem. Ref. Data*, 1985, **14**(suppl. 1), 1270–1293.
- 46 J. Zheng, J. L. Bao, R. Meana-Pañeda, S. Zhang, B. J. Lynch, J. C. Corchado, Y.-Y. Chuang, P. L. Fast, W.-P. Hu, Y.-P. Liu, G. C. Lynch, K. A. Nguyen, C. F. Jackels, A. F. Ramos, B. A. Ellingson, V. S. Melissas, J. Villà, I. Rossi, E. L. Coitiño, J. Pu and T. V. Albu, *POLYRATE, version 9.7, Department of Chemistry and Supercomputing Institute*, University of Minnesota, Minneapolis, Minnesota 55455, 2007.
- 47 J. J. Sloan, D. G. Watson and J. Williamson, *Chem. Phys. Lett.*, 1980, **74**, 481–485.
- 48 D. J. Douglas and J. J. Sloan, *Chem. Phys.*, 1980, **46**, 307–312.